upregulates Sox2 expression through association with its enhancer region.

Sox4 Is An Essential Factor for Maintenance of Stemness of Glioma-Initiating Cells

So far, Sox4 has not been reported to have any role in maintenance of stem cell properties. To study the role of Sox4 in glioma-initiating cells, we examined the effect of Sox4 knockdown on stemness of glioma-initiating cells. Sox4-knockeddown glioma-initiating cells showed less sphere-forming ability and self-renewal capacity (Figures 6A and 6B), and the size of CD133+ pool was decreased (72.6% to 41.5% or 41.1%; Figure 6C). Moreover, the number of Nestin-positive cells was decreased, while that of GFAP-positive cells was increased by Sox4 knockdown (Figure 6D). These results indicate that Sox4 is involved in a crucial pathway for maintenance of stemness of glioma-initiating cells.

Sox4 Plays an Essential Role in Maintenance of Stemness of Glioma-Initiating Cells by TGF-β

From these results, we hypothesized that Sox4 expression directly induced by TGF-β promotes Sox2 expression and maintains stemness of glioma-initiating cells. To test this hypothesis, first, we examined the effect of TGF-β inhibitor on glioma-initiating cells infected with adenovirus carrying cDNA of Sox4. Sox4-overexpressing glioma-initiating cells showed resistance against deprivation of sphere-forming ability by SB431542 (Figure 7A). Moreover, the number of Nestin-positive cells and that of GFAP-positive cells of Sox4-overexpressed glioma-initiating cells were minimally affected by SB431542 (Figure 7B). These data suggest that direct induction of Sox4 expression by TGF-β plays essential roles in maintenance of stemness of glioma-initiating cells.

TGF-β Inhibitor Deprives Glioma-Initiating Cells of In Vivo Tumorigenic Activity through Downregulation of Sox4 Expression

To study the role of TGF-β-induced Sox4 in maintenance of stemness in vivo, we examined the effects of TGF-β inhibitor and Sox4 on intracranial growth of glioma-initiating cells (Figure 7C). As TGF-β is well known to promote proliferation of bulk glioma cells, SB431542 was used in pretreatment, rather than successive treatment, to distinguish the effect on differentiation from that on proliferation. The survival of the mice inoculated with SB431542-pretreated glioma-initiating cells was significantly prolonged compared to mice injected with control glioma-initiating cells. All mice bearing control glioma-initiating cells developed neurological signs and displayed large tumors. In contrast, all mice bearing SB431542-pretreated glioma-initiating cells did not develop neurological signs and the brains showed no evidence of tumor by pathological examination with H&E staining. Furthermore, the survival advantage effect of SB431542 was not observed for Sox4-transduced glioma-initiating cells (Figure 7C). Altogether, we concluded that TGF-β upregulates Sox2 expression through direct induction of Sox4 to sustain stemness of glioma-initiating cells and that TGF-β inhibitor blocks this pathway to deprive them of aggressiveness (Figure 7D).
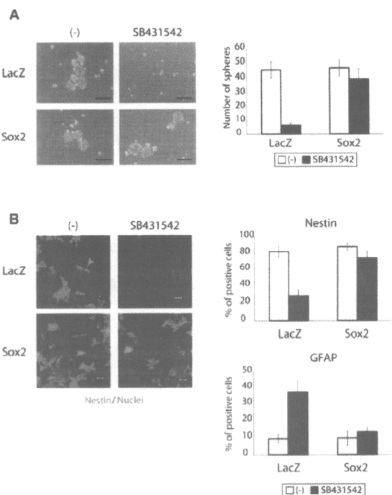
Figure 3. Downregulation of Sox2 Expression by TGF-β Inhibitor Is a Critical Step for Differentiation of Glioma-Initiating Cells

(A) Representative images of TGS-01 cells infected with adenovirus-Sox2 or LacZ (negative control) and cultured with or without SB431542 (1 μM) for 7 days. The data are presented as the number of glioma spheres formed (means ± SEM of five fields). Scale bars, 100 μm.

(B) Marker expression of TGS-01 cells infected with adenovirus-Sox2 or LacZ and cultured with or without SB431542 (1 μM) for 7 days. Images of Nestin-positive cells are shown in the left panels. Quantification of Nestin-positive or GFAP-positive cells among total cells is shown in the right graphs. Error bars represent SEM. Scale bars, 20 μm.

DISCUSSION

TGF-β was reported to induce epithelial-mesenchymal transition (EMT) in immortalized human mammary epithelial cells and increase the ability to form mammospheres (Mani et al., 2008). These findings suggest a direct link between EMT and the gain of epithelial stem cell properties of carcinoma. Such a link could be applied to other carcinoma stem cells than breast CSCs. However, since glioma cells per se have nonepithelial characters, the link may not be applied to GSCs.

To analyze roles of TGF-β signaling in glioma stem cells, we have used glioma tissues obtained from patients with GBM and they were cultured in serum-free medium ("sphere"). All of the ten mice injected intracranially with 5 × 10³ TGS-01 "sphere" cells were killed within 70 days after transplantation, while all of the ten mice bearing 5 × 10⁵ matched "differentiated" cells had survived for more than 140 days without neurological signs (M.T., Y.I., and T.T., unpublished data). These results indicate that populations with a higher tumorigenic activity were enriched in "sphere" cells.
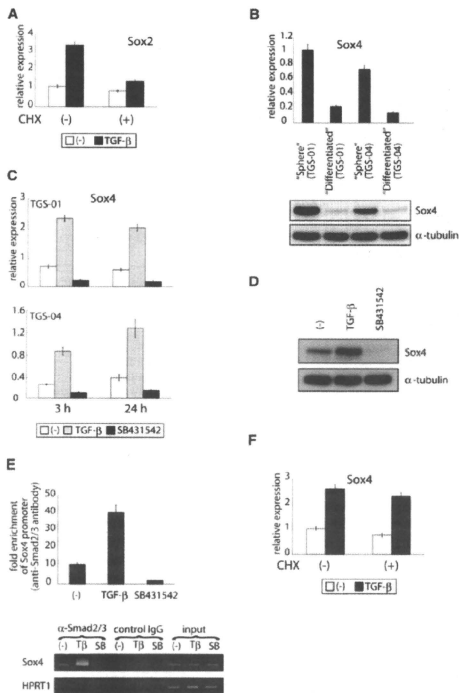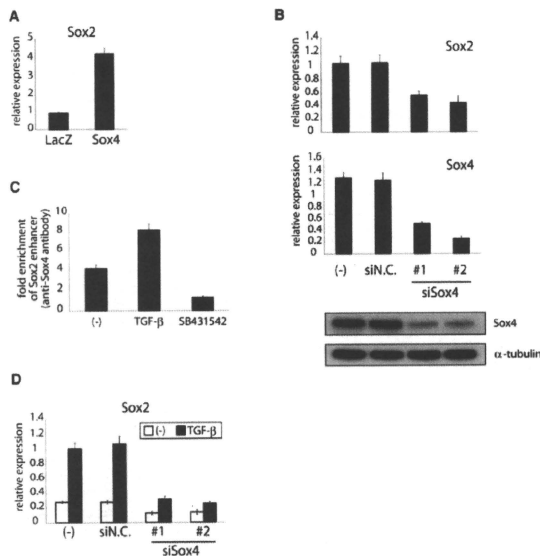
Figure 4. Sox4 Is a Direct Target Gene of TGF-β Signaling

(A) Expression levels of Sox2 mRNA after TGF-β (100 pM) treatment for 24 hr. Treatment with cycloheximide (CHX, 3 μg/ml) was started 30 min before stimulation with TGF-β. Values were normalized to amounts of GAPDH mRNA. Error bars represent SEM.

(B) Expression levels of Sox4 mRNA and protein in "Sphere" cells and "Differentiated" cells. α-tubulin was used as a loading control.

(C) Amount of Sox4 mRNA was determined after TGF-β ligand (100 pM) or inhibitor (SB431542, 1 μM) treatment for 3 or 24 hr. Values were normalized to that of GAPDH mRNA. Error bars represent SEM.

(D) Amount of Sox4 protein was determined after TGF-β ligand (100 pM) or inhibitor (SB431542, 1 μM) treatment for 24 hr. α-tubulin was used as a loading control.

(E) Association of Smad complex with the Sox4 promoter. Chromatin immunoprecipitation analysis was performed using TGS-01 cells treated with TGF-β ligand (100 pM) or inhibitor (SB431542, 1 μM) for 1.5 hr. Eluted DNAs were subjected to quantitative real-time PCR analysis (graph) or conventional RT-PCR (figure). In real-time PCR analysis, values were normalized to the amount of the first intron of hypoxanthine phosphoribosyltransferase (HPRT) 1. Error bars represent SEM. Input, 1%.

(F) Expression levels of Sox4 were analyzed using cDNAs, which were prepared in the experiments shown in (A).

We have shown here that inhibition of TGF-β signaling induces differentiation of glioma-initiating cells and that TGF-β maintains stemness of these cells through induction of Sox2 expression. Moreover, we have demonstrated that Sox4 is a direct target of TGF-β and that Sox4 mediates TGF-β-induced Sox2 expression. Although inhibition of TGF-β signaling markedly promoted differentiation of glioma-initiating cells, addition of TGF-β failed to induce substantial change in glioma-initiating cells. It may be because TGF-β ligand is sufficiently produced by glioma-initiating cells for maintenance of their stemness at the basal level (Figure S5) in spite of the findings that TGF-β signaling itself is not saturated (Figures 2A, 2C, 4C, and 4D). Consistent with these results, overexpression of Sox4 or Sox2 in glioma-initiating cells did not affect their sphere-forming ability in the presence of autocrine TGF-β signaling. These results indicate that in glioma-initiating cells Sox4 and Sox2 are present at sufficient levels for retention of their aggressiveness in the presence of autocrine TGF-β signaling.

Bone morphogenetic protein (BMP) 4, another member of the TGF-β family, promotes differentiation and depletes the pool of glioma-initiating cells (Piccirillo et al., 2006). BMP signaling is known to control the activity of normal brain stem cells (Lim et al., 2000), and TGF-β signaling also regulates normal brain development (Golestaneh and Mishra, 2005; Muñoz-Sanjuán and Brivanlou, 2002). Altogether, the roles of TGF-β and BMP signaling in GSCs may reflect those in normal NSCs, supporting the concept that GSCs and NSCs are closely related (Vescovi et al., 2006).

Sox2 is well known to be one of the self-renewal genes, such as Oct4 and Nanog, and to play pivotal roles in maintaining stemness of embryonic stem cells (Kamachi et al., 2000). Sox2 null mutant embryos cannot give rise to embryonic or trophectoderm lineages (Gubbay et al., 1990). Introduction of Sox2 together with Oct4, Klf4, and c-Myc to human or mouse adult fibroblasts results in generation of induced pluripotent stem (iPS) cells (Takahashi and Yamanaka, 2006; Takahashi et al., 2007). Sox2 also plays essential roles in maintenance of NSCs (Graham et al., 2003), and Sox2 deficiency causes impaired neurogenesis in adult mouse brain (Ferri et al., 2004). Although it was reported that glioma tissues highly express Sox2 mRNA compared to nonmalignant tissues (Ben-Porath et al., 2008; Schmitz et al., 2007), the role of Sox2 in the development of glioma has not yet been determined. In glioma cells, expression levels of Sox2 are linearly and exponentially correlated with those of Nestin and CD133, respectively (Figure S11A, data set from Lee et al., 2006). Here, we demonstrated that knockdown of Sox2 resulted in deprivation of tumorigenic activity of glioma-initiating cells. Our report is the first to show significance of Sox2 in development of glioma and maintenance of the aggressive characters of glioma cells. The results that Sox2 is an essential factor for

− 399 −

Figure 5. Sox4 Is a Crucial Mediator for TGF-β-Induced Sox2 Expression

(A) Effects of Sox4 overexpression on expression of Sox2. TGS-01 cells were infected with adeno-virus-Sox4 or LacZ 24 hr before harvest. Values were normalized to the amount of GAPDH mRNA. Error bars represent SEM.

(B) Effects of Sox4 knockdown on expression of Sox2. Upper graphs show mRNA levels of Sox2 and Sox4. RNA levels were normalized to amounts of GAPDH mRNA. Error bars represent SEM. Lower panels show protein levels of Sox4 and α-tubulin.

(C) Association of Sox4 with the Sox2 enhancer. Chromatin immunoprecipitation analysis was performed using TGS-01 cells treated with TGF-β ligand (100 pM) or inhibitor (SB431542, 1 μM) for 24 hr. Eluted DNAs were subjected to quantitative real-time PCR analysis. Values were normalized to the amount of the first intron of HPRT1. Error bars represent SEM.

(D) TGF-β-induced Sox2 expression under the condition of Sox4 knockdown. Expression levels of Sox2 mRNA after TGF-β (100 pM) treatment for 24 hr were determined by real-time PCR. Indicated siRNAs were transfected 24 hr before TGF-β treatment.

noma, prostate cancer, lung cancer, bladder carcinoma, and medulloblastoma (Aaboe et al., 2006; Lee et al., 2002; Liao et al., 2008; Liu et al., 2006b; Pramoonjago et al., 2006; Yokota et al., 2004). The mechanism of Sox4 function as an oncogene, however, has not been fully investigated. From our report, Sox4 can be defined as an oncogene with new mechanisms, at least in glioblastoma.

Although we demonstrated that the TGF-β-Sox4-Sox2 pathway is indispensable for the maintenance of stemness of glioma-initiating cells, the possibility cannot be excluded that other signaling pathways are also involved in it. Hedgehog signaling has been implicated in the development of glioma for many years. It was reported that Hedgehog-Gli1 pathway regulates the stemness of glioma-initiating cells and that cyclopamine, a hedgehog inhibitor, could reduce glioma tumor volume (Clement et al., 2007), though the mechanisms by which inhibition of Hedgehog-Gli1 pathway promotes differentiation of glioma-initiating cells were not investigated. Cyclopamine abrogated sphere-forming ability of TGS-01 cells, but this effect was weaker than that of SB431542, and these two agents failed to show additive or synergistic effects (Figure S12). Therefore, it is likely that there are at least two types of GSCs, Hedgehog-Gli1 pathway-dependent cells and TGF-β-Sox4-Sox2 pathway-dependent cells. To apply Hedgehog inhibitor and TGF-β inhibitor to clinical stages, it will be necessary to assess GSCs of each patient for their signal dependency.

While this manuscript was under revision, Peñuelas et al. (2009) independently reported that TGF-β increases glioma-initiating cell self-renewal through induction of LIF in human glioblastoma. Their results agree with our report in terms of the role

maintenance of GSCs as well as NSCs and embryonic stem cells support the concept that malignant cancer cells and normal developing cells are closely associated with each other in their biological properties. Because Sox2 is a crucial factor for maintenance of other tissue stem cells, it can be speculated that Sox2 also plays significant roles in maintenance of other CSCs.
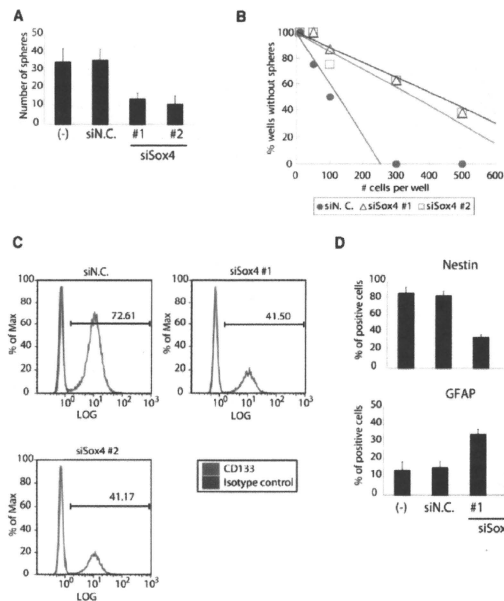
Although Sox2 is already known to play crucial roles to maintain stemness of NSCs, Sox4 has not been reported to have any function in stem cell properties. So far, Sox4 was reported to be overexpressed in glioma tissues compared to normal brain tissues (Tso et al., 2006), but its role in the development of glioma has not been determined. Here, we have demonstrated that Sox4 binds to Sox2 enhancer region and plays important roles in sustaining tumorigenicity of glioma-initiating cells. From public data sets, we found that glioma-initiating cells show higher expression of Sox2 and Sox4 and that their expression levels significantly correlate with each other (Figures S11B and S11C, data set from Lee et al., 2006), suggesting that the TGF-β-Sox4-Sox2 pathway is widely used in glioma-initiating cells for retention of their stemness. These findings may add a new player, Sox4, to the concept of stemness.

Sox4 contains a DNA-binding domain known as the HMG box and has been shown to be a transcriptional activator involved in the development of the cardiac outflow tract and the central nervous system (Cheung et al., 2000). So far, Sox4 overexpression has been found to be associated with several human cancer types, including not only glioma but also hepatic cellular carci-

− 400 −

Figure 6. Sox4 Plays Important Roles in Maintenance of Stemness of Glioma-Initiating Cells

(A) TGS-01 cells were dissociated into single-cell populations, transfected with control or Sox4 siRNA duplex, and cultured for 7 days. The data are presented as the number of glioma spheres formed (means ± SEM of five fields).

(B) Knockdown of Sox4 expression by siRNA in TGS-01 cells resulted in a decrease of self-renewal capacity in limiting dilution assay.

(C) Effects of Sox4 knockdown on CD133+ subpopulation of TGS-01 cells were determined by flow cytometry.

(D) Quantification of Nestin-positive or GFAP-positive cells among total cells. Differentiation of TGS-01 cells by Sox4 knockdown was analyzed 7 days after transfection of control (N.C.) or Sox4 siRNA duplex. Error bars represent SEM.

EXPERIMENTAL PROCEDURES

Cell Culture and Reagents

Primary grade IV glioblastoma samples were obtained during surgery from consenting patients, as approved by the Institutional Review Board at the University of Tokyo Hospital (Characteristics of the patients are listed in Figure S1A). Spheres were cultured in DMEM/F12 serum-free medium (Invitrogen) supplemented with B27 (Invitrogen), 20 ng/ml of EGF, and 20 ng/ml of bFGF (both from PeproTech). The antibodies used were as follows: anti-Musashi (Chemicon), anti-Nestin (Chemicon), anti-GFAP (Dako), anti-Tuj1 (Covance), anti-Sox2 (R&D), anti-Sox4 (Santa Cruz), anti-α-tubulin (Sigma-Aldrich), anti-phospho-Smad2 (Zymed Laboratories), anti-Smad2/3 (BD Transduction Laboratories), and phycoerythrin-conjugated CD133/2 (293C3) antibody (Miltenyi Biotec). SB431542 and cyclo-heximide were purchased from Sigma-Aldrich. Recombinant human TGF-β RII/Fc chimera was from R&D Systems.

of TGF-β signaling in maintenance of glioma-initiating cells. Although glioma-initiating cells used in our study, TGS-01 and -04, were deprived of their tumorigenicity in the presence of anti-LIF neutralizing antibody (Figure S13), TGF-β signaling failed to induce LIF expression (Figure S7). Taken together, TGF-β signaling may maintain tumorigenicity of glioma-initiating cells through multiple (at least two) independent pathways.

To target TGF-β signaling in glioma, clinical studies of a TGF-β2-specific antisense oligonucleotide AP 12009 in recurrent or refractory high-grade glioma are ongoing (Schlingensiepen et al., 2006). Our findings indicate that such TGF-β inhibitors should be delivered to GSCs, not only to the tumor bulk. This indication will thus pursue the realization of new therapeutic strategies, inducing differentiation of GSCs in addition to suppressing bulk tumor growth. Classical pharmacological therapies cannot sufficiently eradicate GSCs (Liu et al., 2006a). Moreover, GSCs were known to be resistant against radiotherapy (Bao et al., 2006). Our results raise the possibility that TGF-β inhibitors can be used in a combination therapy with classical pharmacological therapies and radiation to make glioblastoma less aggressive. To achieve this, we need to develop a method for delivery of TGF-β inhibitor to GSCs. Delivery of TGF-β inhibitor to GSCs without affecting the functions of normal brain tissues may improve prognosis of GBM, one of the most lethal malignant tumors.

Immunostaining

Glioma-initiating cells were seeded on poly-L-ornithine (Sigma)- and fibronectin (Sigma)-coated slide glasses and cultured for 7 days with indicated ligands or inhibitors in serum-free medium. Cells were fixed with 3.7% paraformaldehyde, permealized with PBS containing 0.3% Triton X-100, and incubated with indicated antibodies. Subsequently, samples were incubated with secondary antibodies and stained with propidium iodide (Molecular Probes) for nuclear staining. Stained cells were observed with a confocal microscope (LSM510, Carl Zeiss).

Flow Cytometry

Cells were dissociated into single-cell populations and labeled with a phycoerythrin-conjugated CD133 antibody. The expression level was analyzed using a Beckman Coulter EPICS XL flow cytometer with EXPO32 ADC software.
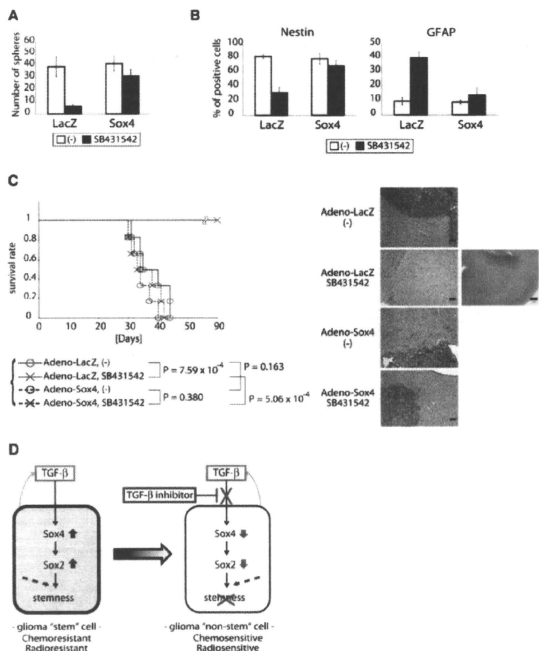
Sphere-Forming Assay

Glioma-initiating cells were cultured in non-tissue-culture-treated flask (BD Biosciences) with vented caps (BD Biosciences) for 7 days. Floated spheres in five fields per each sample were counted under a microscope (magnification, ×40).

RNA Interference

Small interfering RNAs (siRNAs, see Table S1 for sequences) were purchased from Invitrogen and introduced into cells using Oligofectamine transfection reagent (Invitrogen) according to the manufacturer's instructions.

Figure 7. Direct Suppression of Sox4 Expression by TGF-β Inhibitor Is a Critical Step for Differentiation of Glioma-Initiating Cells In Vitro and In Vivo

(A) TGS-01 cells were dissociated into single-cell populations, infected with adenovirus-Sox4 or LacZ, and cultured with or without SB431542 (1 μM) for 7 days. The data are presented as the number of glioma spheres formed (means ± SEM of five fields).

(B) Marker expression of TGS-01 cells infected with adenovirus-Sox4 or LacZ and cultured with or without SB431542 (1 μM) for 7 days. Quantification of Nestin-positive or GFAP-positive cells among total cells is shown in graphs. Error bars represent SEM.

(C) Development of gliomas after intracranial transplantation of 5 × 10^{4} TGS-01 cells infected with adenovirus-Sox4 or LacZ (negative control) and treated with or without TGF-β inhibitor (SB431542, 1 μM) for 24 hr. Survival of mice (n = 6 mice for each condition) was evaluated by Kaplan-Meier analysis (left graph). p value was calculated using a log-rank test. Right panels show the results of histological examination of the samples dissected at 30 days after intracranial transplantation. Tissue sections were stained with hematoxylin and eosin. Scale bars, 50 μm in the four left images (×20) and 300 μm in the right image (×4).

(D) Model of maintenance of stemness of glioma-initiating cells by autocrine TGF-β signaling. TGF-β directly induces Sox4 expression. Subsequently, Sox4 promotes expression of Sox2, which plays significant roles in sustaining stemness of glioma-initiating cells, possibly in cooperation with other signaling pathways (dotted arrows). TGF-β inhibitor blocks this "TGF-β-Sox4-Sox2" pathway, promotes differentiation of glioma-initiating cells, and deprives them of aggressiveness.

Adenoviruses

Flag-tagged full-length Sox2 and Sox4 cDNAs were cloned into a pENTR vector (Invitrogen) and introduced into the adenoviral genome via recombination between pENTR vector and the pAd/CMV/V5-DEST vector using LR Clonase (Invitrogen). HEK293A cells were infected with pAd/CMV/Sox2 or pAd/CMV/Sox4 after linearization of it with PacI. Viral particles were isolated by three freeze-thaw cycles and amplified by reinfection to HEK293A cells.

Cell Lysis and Immunoblotting

Cells were lysed with a buffer containing 1% Nonidet P-40, 20 mM Tris-HCl (pH 7.4), 150 mM NaCl, 1 mM PMSF, 1% aprotinin, and 5 mM EDTA. Proteins in cleared cell lysates were subjected to SDS-PAGE and transferred to Fluoro Trans W membrane (Pall). Immunoblotting was performed using the indicated antibodies.

Quantitative Real-Time PCR

Quantitative real-time reverse transcription PCR was performed as described previously (Ikushima et al., 2008). All samples were run in triplicate in each experiment. The primers used are listed in Table S1. Values were normalized to that for glyceraldehyde-3-phosphate dehydrogenase (GAPDH).

Limiting Dilution Assay

Sphere cells were dissociated and plated in 96-well plates in 200 μl serum-free medium. After a 7 day culture, the percentage of wells not containing spheres

for each cell-plating density was calculated and plotted against the number of cells per well.

Chromatin Immunoprecipitation

Chromatin immunoprecipitation was performed as described previously (Koinuma et al., 2009). Following reverse crosslinking, DNA was treated with proteinase K and purified using a PCR purification kit (QIAGEN). DNA was eluted in 30 μl of TE and used for PCR analysis or quantitative real-time PCR. PCR primers are listed in Table S1.

Intracranial Proliferation Assay

Viable glioma-initiating cells (5 × 10^{4}) in 5 μl of DMEM/F12 medium were injected stereotactically into the right cerebral hemisphere of 5-week-old female BALB/c nu/nu mice at a depth of 3 mm. All animal experimental protocols were performed in accordance with the policies of the Animal Ethics Committee of the University of Tokyo.

Statistical Analysis of Microarray Data

Microarray data were obtained from GEO (http://www.ncbi.nlm.nih.gov/geo/) and ArrayExpress (http://www.ebi.ac.uk/microarray/). Data were analyzed with statistical software R (http://www.R-project.org).

REFERENCES

Aaboe, M., Birkenkamp-Demtroder, K., Wiuf, C., Sørensen, F.B., Thykjaer, T., Sauter, G., Jensen, K.M., Dyrskjøt, L., and Ørntoft, T. (2006). SOX4 expression in bladder carcinoma: clinical aspects and in vitro functional characterization. Cancer Res. 66, 3434–3442.

Bao, S., Wu, Q., McLendon, R.E., Hao, Y., Shi, Q., Hjelmeland, A.B., Dewhirst, M.W., Bigner, D.D., and Rich, J.N. (2006). Glioma stem cells promote radioresistance by preferential activation of the DNA damage response. Nature 444, 756–760.

Beier, D., Hau, P., Proescholdt, M., Lohmeier, A., Wischhusen, J., Oefner, P.J., Aigner, L., Brawanski, A., Bogdahn, U., and Beier, C.P. (2007). CD133(+) and CD133(-) glioblastoma-derived cancer stem cells show differential growth characteristics and molecular profiles. Cancer Res. 67, 4010–4015.

Ben-Porath, I., Thomson, M.W., Carey, V.J., Ge, R., Bell, G.W., Regev, A., and Weinberg, R.A. (2008). An embryonic stem cell-like gene expression signature in poorly differentiated aggressive human tumors. Nat. Genet. 40, 499–507.

Bruna, A., Darken, R.S., Rojo, F., Ocaña, A., Peñuelas, S., Arias, A., Paris, R., Tortosa, A., Mora, J., Baselga, J., et al. (2007). High TGFbeta-Smad activity confers poor prognosis in glioma patients and promotes cell proliferation depending on the methylation of the PDGF-B gene. Cancer Cell 11, 147–160.

Cheung, M., Abu-Elmagd, M., Clevers, H., and Scotting, P.J. (2000). Roles of Sox4 in central nervous system development. Brain Res. Mol. Brain Res. 79, 180–191.

Chew, J.L., Loh, Y.H., Zhang, W., Chen, X., Tam, W.L., Yeap, L.S., Li, P., Ang, Y.S., Lim, B., Robson, P., et al. (2005). Reciprocal transcriptional regulation of Pou5f1 and Sox2 via the Oct4/Sox2 complex in embryonic stem cells. Mol. Cell. Biol. 25, 6031–6046.

Clement, V., Sanchez, P., de Tribolet, N., Radovanovic, I., and Ruiz i Altaba, A. (2007). HEDGEHOG-GLI1 signaling regulates human glioma growth, cancer stem cell self-renewal, and tumorigenicity. Curr. Biol. 17, 165–172.

Derynck, R., and Zhang, Y.E. (2003). Smad-dependent and Smad-independent pathways in TGF-beta family signalling. Nature 425, 577–584.

Ehata, S., Hanyu, A., Hayashi, M., Aburatani, H., Kato, Y., Fujime, M., Saitoh, M., Miyazawa, K., Imamura, T., and Miyazono, K. (2007). Transforming growth factor-beta promotes survival of mammary carcinoma cells through induction of antiapoptotic transcription factor DEC1. Cancer Res. 67, 9694–9703.

Ferri, A.L., Cavallaro, M., Braida, D., Di Cristofano, A., Canta, A., Vezzani, A., Ottolenghi, S., Pandolfi, P.P., Sala, M., DeBiasi, S., et al. (2004). Sox2 deficiency causes neurodegeneration and impaired neurogenesis in the adult mouse brain. Development 131, 3805–3819.

Golestaneh, N., and Mishra, B. (2005). TGF-beta, neuronal stem cells and glioblastoma. Oncogene 24, 5722–5730.

Graham, V., Khudyakov, J., Ellis, P., and Pevny, L. (2003). SOX2 functions to maintain neural progenitor identity. Neuron 39, 749–765.

Gubbay, J., Collignon, J., Koopman, P., Capel, B., Economou, A., Münsterberg, A., Vivian, N., Goodfellow, P., and Lovell-Badge, R. (1990). A gene mapping to the sex-determining region of the mouse Y chromosome is a member of a novel family of embryonically expressed genes. Nature 346, 245–250.

Günther, H.S., Schmidt, N.O., Phillips, H.S., Kemming, D., Kharbanda, S., Soriano, R., Modrusan, Z., Meissner, H., Westphal, M., and Lamszus, K. (2008). Glioblastoma-derived stem cell-enriched cultures form distinct subgroups according to molecular and phenotypic criteria. Oncogene 27, 2897–2909.

Hirschmann-Jax, C., Foster, A.E., Wulf, G.G., Nuchtern, J.G., Jax, T.W., Gobel, U., Goodell, M.A., and Brenner, M.K. (2004). A distinct "side population" of cells with high drug efflux capacity in human tumor cells. Proc. Natl. Acad. Sci. USA 101, 14228–14233.

Ikushima, H., Komuro, A., Isogaya, K., Shinozaki, M., Hellman, U., Miyazawa, K., and Miyazono, K. (2008). An Id-like molecule, HHM, is a synexpression group-restricted regulator of TGF-β signalling. EMBO J. 27, 2955–2965.

Inman, G.J., Nicolás, F.J., Callahan, J.F., Harling, J.D., Gaster, L.M., Reith, A.D., Laping, N.J., and Hill, C.S. (2002). SB-431542 is a potent and specific inhibitor of transforming growth factor-beta superfamily type I activin receptor-like kinase (ALK) receptors ALK4, ALK5, and ALK7. Mol. Pharmacol. 62, 65–74.

Kamachi, Y., Uchikawa, M., and Kondoh, H. (2000). Pairing SOX off: with partners in the regulation of embryonic development. Trends Genet. 16, 182–187.

Koinuma, D., Tsutsumi, S., Kamimura, N., Taniguchi, H., Miyazawa, K., Sunamura, M., Imamura, T., Miyazono, K., and Aburatani, H. (2009). Chromatin immunoprecipitation on microarray analysis of Smad2/3 binding sites reveals roles of ETS1 and TFAP2A in transforming growth factor beta signaling. Mol. Cell. Biol. 29, 172–186. Published online October 27, 2008. 10.1128/MCB.01038-08.

Kondo, T., Setoguchi, T., and Taga, T. (2004). Persistence of a small subpopulation of cancer stem-like cells in the C6 glioma cell line. Proc. Natl. Acad. Sci. USA 101, 781–786.

Lee, C.J., Appleby, V.J., Orme, A.T., Chan, W.I., and Scotting, P.J. (2002). Differential expression of SOX4 and SOX11 in medulloblastoma. J. Neurooncol. 57, 201–214.

Lee, J., Kotliarova, S., Kotliarov, Y., Li, A., Su, Q., Donin, N.M., Pastorino, S., Purow, B.W., Christopher, N., Zhang, W., et al. (2006). Tumor stem cells derived from glioblastomas cultured in bFGF and EGF more closely mirror the phenotype and genotype of primary tumors than do serum-cultured cell lines. Cancer Cell 9, 391–403.

Liao, Y.L., Sun, Y.M., Chau, G.Y., Chau, Y.P., Lai, T.C., Wang, J.L., Horng, J.T., Hsiao, M., and Tsou, A.P. (2008). Identification of SOX4 target genes using phylogenetic footprinting-based prediction from expression microarrays suggests that overexpression of SOX4 potentiates metastasis in hepatocellular carcinoma. Oncogene 27, 5578–5589.

Lim, D.A., Tramontin, A.D., Trevejo, J.M., Herrera, D.G., García-Verdugo, J.M., and Alvarez-Buylla, A. (2000). Noggin antagonizes BMP signaling to create a niche for adult neurogenesis. Neuron 28, 713–726.

Liu, G., Yuan, X., Zeng, Z., Tunici, P., Ng, H., Abdulkadir, I.R., Lu, L., Irvin, D., Black, K.L., and Yu, J.S. (2006a). Analysis of gene expression and chemoresistance of CD133+ cancer stem cells in glioblastoma. Mol. Cancer 5, 67.

Liu, P., Ramachandran, S., Ali Seyed, M., Scharer, C.D., Laycock, N., Dalton, W.B., Williams, H., Karanam, S., Datta, M.W., Jaye, D.L., et al. (2006b). Sex-determining region Y box 4 is a transforming oncogene in human prostate cancer cells. Cancer Res. 66, 4011–4019.

Mani, S.A., Guo, W., Liao, M.J., Eaton, E.N., Ayyanan, A., Zhou, A.Y., Brooks, M., Reinhard, F., Zhang, C.C., Shipitsin, M., et al. (2008). The epithelial-mesenchymal transition generates cells with properties of stem cells. Cell 133, 704–715.

Massagué, J. (2008). TGFbeta in cancer. Cell 134, 215–230.

Matsuyama, S., Iwadate, M., Kondo, M., Saitoh, M., Hanyu, A., Shimizu, K., Aburatani, H., Mishima, H.K., Imamura, T., Miyazono, K., et al.(2003). SB-431542 and

Gleevec inhibit transforming growth factor-beta-induced proliferation of human osteosarcoma cells. Cancer Res. 63, 7791–7798.

Miyazawa, K., Shinozaki, M., Hara, T., Furuya, T., and Miyazono, K. (2002). Two major Smad pathways in TGF-beta superfamily signalling. Genes Cells 7, 1191–1204.

Muñoz-Sanjuán, I., and Brivanlou, A.H. (2002). Neural induction, the default model and embryonic stem cells. Nat. Rev. Neurosci. 3, 271–280.

Peñuelas, S., Anido, J., Prieto-Sánchez, R.M., Folch, G., Barba, I., Cuartas, I., García-Dorado, D., Poca, M.A., Sahuquillo, J., Baselga, J., et al. (2009). TGF-beta increases glioma-initiating cell self-renewal through the induction of LIF in human glioblastoma. Cancer Cell 15, 315–327.

Piccirillo, S.G., Reynolds, B.A., Zanetti, N., Lamorte, G., Binda, E., Broggi, G., Brem, H., Olivi, A., Dimeco, F., and Vescovi, A.L. (2006). Bone morphogenetic proteins inhibit the tumorigenic potential of human brain tumour-initiating cells. Nature 444, 761–765.

Pramoonjago, P., Baras, A.S., and Moskaluk, C.A. (2006). Knockdown of Sox4 expression by RNAi induces apoptosis in ACC3 cells. Oncogene 25, 5626–5639.

Sánchez-Capelo, A. (2005). Dual role for TGF-beta1 in apoptosis. Cytokine Growth Factor Rev. 16, 15–34.

Sawyer, J.S., Anderson, B.D., Beight, D.W., Campbell, R.M., Jones, M.L., Herron, D.K., Lampe, J.W., McCowan, J.R., McMillen, W.T., Mort, N., et al. (2003). Synthesis and activity of new aryl- and heteroaryl-substituted pyrazole inhibitors of the transforming growth factor-beta type I receptor kinase domain. J. Med. Chem. 46, 3953–3956.

Schlingensiepen, K.H., Schlingensiepen, R., Steinbrecher, A., Hau, P., Bogdahn, U., Fischer-Blass, B., and Jachimczak, P. (2006). Targeted tumor therapy with the TGF-beta2 antisense compound AP 12009. Cytokine Growth Factor Rev. 17, 129–139.

Schmitz, M., Temme, A., Senner, V., Ebner, R., Schwind, S., Stevanovic, S., Wehner, R., Schackert, G., Schackert, H.K., Fussel, M., et al. (2007). Identification of SOX2 as a novel glioma-associated antigen and potential target for T cell-based immunotherapy. Br. J. Cancer 96, 1293–1301.

Singh, S.K., Hawkins, C., Clarke, I.D., Squire, J.A., Bayani, J., Hide, T., Henkelman, R.M., Cusimano, M.D., and Dirks, P.B. (2004). Identification of human brain tumour initiating cells. Nature 432, 396–401.

Surawicz, T.S., Davis, F., Freels, S., Laws, E.R., and Menck, H.R. (1998). Brain tumor survival: results from the National Cancer Data Base. J. Neurooncol. 40, 151–160.

Takahashi, K., Tanabe, K., Ohnuki, M., Narita, M., Ichisaka, T., Tomoda, K., and Yamanaka, S. (2007). Induction of pluripotent stem cells from adult human fibroblasts by defined factors. Cell 131, 861–872.

Takahashi, K., and Yamanaka, S. (2006). Induction of pluripotent stem cells from mouse embryonic and adult fibroblast cultures by defined factors. Cell 126, 663–676.

Tojo, M., Hamashima, Y., Hanyu, A., Kajimoto, T., Saitoh, M., Miyazono, K., Node, M., and Imamura, T. (2005). The ALK-5 inhibitor A-83–01 inhibits Smad signaling and epithelial-to-mesenchymal transition by transforming growth factor-beta. Cancer Sci. 96, 791–800.

Tomioka, M., Nishimoto, M., Miyagi, S., Katayanagi, T., Fukui, N., Niwa, H., Muramatsu, M., and Okuda, A. (2002). Identification of Sox-2 regulatory region which is under the control of Oct-3/4-Sox-2 complex. Nucleic Acids Res. 30, 3202–3213.

Tso, C.L., Shintaku, P., Chen, J., Liu, Q., Liu, J., Chen, Z., Yoshimoto, K., Mischel, P.S., Cloughesy, T.F., Liau, L.M., et al. (2006). Primary glioblastomas express mesenchymal stem-like properties. Mol. Cancer Res. 4, 607–619.

Vescovi, A.L., Galli, R., and Reynolds, B.A. (2006). Brain tumour stem cells. Nat. Rev. Cancer 6, 425–436.

Xu, R.H., Sampsell-Barron, T.L., Gu, F., Root, S., Peck, R.M., Pan, G., Yu, J., Antosiewicz-Bourget, J., Tian, S., Stewart, R., et al. (2008). NANOG is a direct target of TGFbeta/activin-mediated SMAD signaling in human ESCs. Cell Stem Cell 3, 196–206.

Yokota, N., Mainprize, T.G., Taylor, M.D., Kohata, T., Loreto, M., Ueda, S., Dura, W., Grajkowska, W., Kuo, J.S., and Rutka, J.T. (2004). Identification of differentially expressed and developmentally regulated genes in medulloblastoma using suppression subtraction hybridization. Oncogene 23, 3444–3453.

−404−

ELSEVIER

doi:10.1016/j.ijrobp.2009.05.065

PHYSICS CONTRIBUTION

THE DEVELOPMENT AND CLINICAL USE OF A BEAM ON-LINE PET SYSTEM MOUNTED ON A ROTATING GANTRY PORT IN PROTON THERAPY

Teiji Nishio, Ph.D.,[*][†] Aya Miyatake, M.Sc.,[‡] Takashi Ogino, M.D.,[*] Keiichi Nakagawa, M.D.,[†] Nagahiro Saijo, M.D.,[§] and Hiroyasu Esumi, M.D.[||]

From the [*]Particle Therapy Division, Research Center for Innovative Oncology, National Cancer Center, Kashiwa; [†]Department of Radiology, Graduate School of Medicine, University of Tokyo; [‡]Department of Nuclear Engineering and Management, Graduate School of Engineering, University of Tokyo; [§]Deputy Director, National Cancer Center, Kashiwa; and [||]Director, National Cancer Center, Kashiwa

Purpose: To verify the usefulness of our developed beam ON-LINE positron emission tomography (PET) system mounted on a rotating gantry port (BOLPs-RGp) for dose–volume delivery-guided proton therapy (DGPT).
Methods and Materials: In the proton treatment room at our facility, a BOLPs-RGp was constructed so that a planar PET apparatus could be mounted with its field of view covering the iso-center of the beam irradiation system. Activity measurements were performed in 48 patients with tumors of the head and neck, liver, lungs, prostate, and brain. The position and intensity of the activity were measured using the BOLPs-RGp during the 200 s immediately after the proton irradiation.
Results: The daily measured activity images acquired by the BOLPs-RGp showed the proton irradiation volume in each patient. Changes in the proton-irradiated volume were indicated by differences between a reference activity image (taken at the first treatment) and the daily activity-images. In the case of head-and-neck treatment, the activity distribution changed in the areas where partial tumor reduction was observed. In the case of liver treatment, it was observed that the washout effect in necrotic tumor cells was slower than in non-necrotic tumor cells.
Conclusions: The BOLPs-RGp was developed for the DGPT. The accuracy of proton treatment was evaluated by measuring changes of daily measured activity. Information about the positron-emitting nuclei generated during proton irradiation can be used as a basis for ensuring the high accuracy of irradiation in proton treatment. © 2010 Elsevier Inc.

Dose–volume delivery guided proton therapy (DGPT), Beam ON-LINE PET system on rotating gantry port (BOLPs-RGp), Target nuclear fragment reaction.

INTRODUCTION

Proton therapy is a form of radiotherapy that enables the concentration of a dose onto a tumor by the use of a scanned or modulated Bragg peak. Therefore, it is very important to evaluate the proton-irradiated volume accurately.

Recently, to ensure the high accuracy of proton therapy, imaging studies of positron-emitting nuclei that are generated by target nuclear fragment reactions involving incident protons and nuclei from a patient's body have been performed (1–14). The annihilation gamma rays from the positron-emitting nuclei were measured by a positron emission tomography (PET) system (specifically a beam OFF-LINE PET

system using commercial PET apparatus or PET-computed tomography [CT] apparatus postirradiation or a beam ON-LINE PET system in a proton treatment room). The beam OFF-LINE PET system using the commercial PET-CT apparatus has the advantage of being able to easily acquire fusion images and the ability to reconstruct three-dimensional images. However, the time required for the movement of the patient to the PET room (10–30 min) and the resulting deterioration of the statistical accuracy of the acquired data are large disadvantages. With the beam ON-LINE PET system, capturing a large view and the acquisition of three-dimensional images are difficult because of geometrical problems caused by the beam direction and the PET apparatus (7, 15, 16).

277

The ability to take daily PET images with a high statistical accuracy while the patient remains in the proton irradiation room is a large advantage. Besides, availability of a cone beam (CB) CT system or CT apparatus in the irradiation room can offer the possibility of daily and in situ monitoring of the patient's anatomy. A prototype beam ON-LINE PET system (BOLPs) was previously constructed for basic research (10), and verification of the proton-irradiated volume in a patient's body was confirmed using a PET apparatus and a PET-CT apparatus (beam OFF-LINE PET system) (13).

A BOLPs mounted on a rotating gantry port (BOLPs-RGp) was constructed in our proton treatment room. Activity measurement and PET imaging were performed in 48 patients with tumors of the head and neck, liver, lungs, prostate, and brain during proton treatment at our facility. The position and intensity of the activity were measured daily using the BOLPs-RGp immediately after proton irradiation. Using the activity measurement, we were able to confirm whether the proton beam irradiation of the tumor was reproducibly performed during the treatment period. Moreover, changes in the activity distribution were observed as the volume of the tumor changed, and these changes were related to the delivery dose, changes in the body shape and position of the patient, and the physiologic changes. The PET images from the BOLPs-RGp were sufficient to provide high-quality proton treatment.

METHODS AND MATERIALS

Design of a beam ON-LINE PET system mounted on an RGp

Via the detection of pairs of annihilation gamma rays emitted from the generated radioactive nuclei of a patient's body, the BOLPs-RGp is designed to determine the position and activity of the positron-emitting nuclei generated in patients by proton irradiation. Figure 1 is a picture of the BOLPs-RGp. The BOLPs-RGp was developed as a standardized system for use with proton therapy devices. During proton therapy, the detector heads have many degrees of freedom and the system allows remote control adaptation to each new proton beam condition and a patient's position. As a result, measurement of the activity distribution is simple.

A planar positron imaging system (Hamamatsu Photonics K. K., Hamamatsu, Japan) (17) was newly arranged for the BOLPs-RGp. In comparison to the system used previously (10), the 24 detector units mounted on each detector head were increased to 36 detector units, and each unit was composed of 11×10 arrays of BGO ($Bi_4Ge_3O_{12}$) crystals with a crystal size of $2 \times 2 \times 20$ mm^3. Furthermore, the 2,400 crystals were increased to 3,600 crystals. The gap of each unit became 3.3 mm from 11.0 mm for minimizing dead space in the detector. The field of view (FOV) became 164.8×167.0 mm^2 from 120.8×186.8 mm^2. The maximum field size is 185.0×185.0 mm^2 in the rotating gantry port with the BOLPs-RGp. Therefore, the FOV can almost cover each treatment site of the head and neck, liver, lungs, prostate, and brain for a proton treatment in our facility. However, in case of prostate, the depth activity distribution is not measured in the entrance of the incident proton beam. The BOLPs-RGp was mounted on and the center of its detection area was aligned with the iso-center of the rotating gantry in the treatment room of the proton therapy facility at our center. A PET image reconstructed by a back-projection method
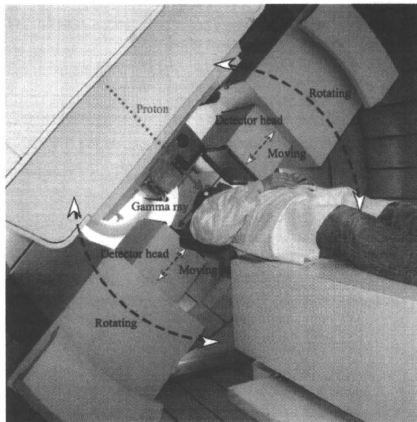

Fig. 1. Setup of the BOLPs-RGp, which is mounted on the rotating gantry port of our proton treatment room.

along the axis of the proton beam direction is always included in the FOV of the opposing detectors together with the axis of the rotating angle of the gantry system. The distance between the two opposing detector heads of the BOLPs-RGp can be adjusted from 30 to 100 cm. When the activity is not being measured, the detector head is stored inside the wall of the gantry device. The position resolution of this system is about 2 mm for the full width at half maximum in the case of use of ^{22}Na point source. The maximum data collection rate for the coincident detection of pair annihilation gamma rays is about 4,000 counts/s/cm^2 (kcps/cm^2). The accuracy of the measurements of activity distribution by this system was verified by a prototype beam ON-LINE PET system (10). The measured data are stored using in the software's list mode format. The activity image is renewed every second. The information of the on-off time points of beam irradiation is recorded in the data, and the image can be restructured according to this information. The PET data from the irradiation field of each patient are managed throughout each treatment day.

The detection efficiency of the distance between the detector heads was calibrated by using the thin-flat acrylic container filled with ^{18}F-solution. The calibration is used for a correction of the imaging uniformity and the detection sensitivity. The attenuation coefficient of 511-keV gamma rays in the patient's body was calculated by the patient's CT image data. They are used for a construction of the activity imaging. The correction of the photon scattering in the patient's body is not considered for the activity imaging. Furthermore, the photons scattered in the patient's body outside the FOV are detected by the effect of the geometry of the detector head. Therefore, the activity image is contaminated by about 10% background in this system. As the result, the position resolution of the activity distribution will become large more than 2 mm in the clinical case of a proton therapy.

Activity measurement in a patient during proton treatment

The measurement of activity was performed daily in 48 cases involving tumors of the head and neck, liver, lungs, prostate, and brain

using the BOLPs-RGp. The position and intensity of activity were measured during the 200 s immediately after proton irradiation using the trigger signal of the beam-off time. The measurement was performed using the shortest possible distance between the two opposing detector heads of the BOLPs-RGp for each patient. The average distance of the detector heads was 40 cm for the head and neck and the brain, 70 cm for the liver and the lungs, and 50 cm for the prostate. The time of 200 s after proton beam irradiation was chosen according to the intensity of activity estimated from the results of other studies (10, 13). The activity data obtained during proton irradiation were not used for PET imaging. Various types of background radiation (X-rays, gamma rays, and neutrons) occur during proton beam irradiation, and the quality of the activity image becomes markedly worse in their presence (2, 10, 15, 16). Furthermore, high radiation decreases the accuracy of the detector.

Verification of activity measurement was performed in 18, 4, 15, 10, and 1 cases involving tumors of the head and neck, the liver, lungs, the prostate, and the brain, respectively. The typical fractional dose is 2.5 Gy equivalents (GyE = Gy × the relative biologic effectiveness: [= 1.1 = constant]) for the head and neck, 3.8 GyE for the liver, 4.0 GyE for the lungs, 2.0 GyE for the prostate, and 2.5 GyE for the brain in our facility. The irradiated field is typically planned with three fields in the head and neck and two fields in other sites. Furthermore, the typical number of irradiated field per fractional dose is one in the head and neck, liver, and prostate, and two in the lungs. The fractional dose was delivered over an irradiation time of 10–300 s. The proton beam irradiation was synchronized with the organ motion caused by respiration in the liver and the lungs.

Procedure for clinical use of activity image

A flow chart of procedure for clinical use of the BOLPs-RGp is shown in Fig. 2. In the clinical use, the main operation is to take an activity image every day and compare the activity image of the first day of treatment with each activity image during the comparatively long period of the treatment. If the difference of both the images is confirmed by reducing of the tumor size and changing of the body shape, then the new dose distribution is obtained from redose calculation of the plan on a new CT image acquisition, and the first proton treatment plan is immediately corrected to the new plan. As a result, proton treatments of high accuracy can be offered to the patient by keeping of the planned dose delivery.

RESULTS

Estimation of the measurement time for PET imaging

An estimation of an appropriate measurement time for PET imaging was performed using the measured activity data from tumors of the head and neck. The proton beam conditions were as follows: an energy of 120 MeV, a spread out of Bragg peak (SOBP) of 80-mm width, a gantry angle of 340°, a fractional dose of 2.5 GyE, and an irradiation time of 24 s. The distance between the detector heads was 70 cm, and the detection rate of the activity was 1.5 kcps. The left panel of Fig. 3 shows the number of detection events per volume during the detection period after proton beam irradiation. The statistical error (= standard deviation/mean value) decreased as the detection time increased. The error was 2.8% for a 200-s detection time, 3.0% for 150 s, 3.4% for 100 s, and 4.4% for 50 s. The right panel of Fig. 3 shows
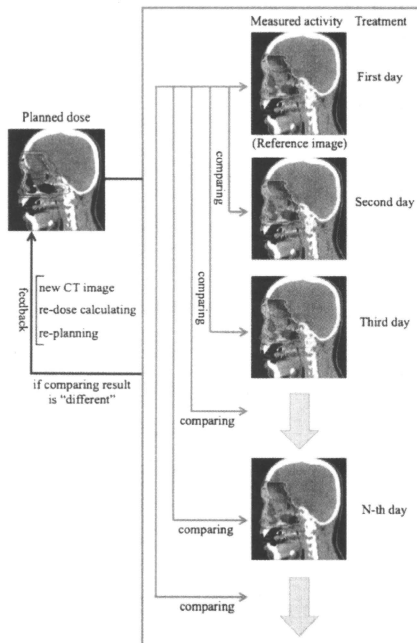

Fig. 2. Flow diagram of the procedure for the clinical use of the BOLPs-RGp.

PET images taken using detection times of (a) 0, (b) 50, (c) 100, and (d) 200 s.

PET images of each treatment site

Typical PET images obtained by the BOLPs-RGp are shown for each case involving tumors of the head and neck, the liver, the lungs, the prostate, and the brain. Figure 4 shows the calculated dose distribution and the measured activity distribution on the first treatment day. The beam irradiation parameters were shown in Table 1. The PET images were obtained during the 200 s after proton beam irradiation. The mean detection rates of the activity generated in the proton beam irradiated volume were 1.58, 1.39, 0.53, 1.08, and 1.85 kcps, respectively. The color line and wash normalized to the iso-center show the dose distribution and activity distribution, respectively. By comparing and verifying between the calculated dose distribution and the measured activity distribution, it can be confirmed visually and roughly that the proton beam has irradiated the tumor. In cases of the liver and the lungs, the length of beam irradiation time is adjusted according to the stability of respiration on the treatment day and the patient. By the effect of organ motion, the number of
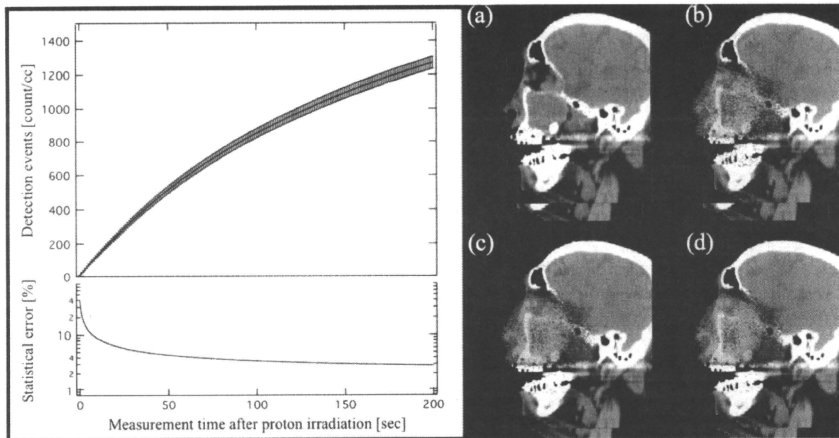
Fig. 3.   The number of detection events per volume and PET images obtained during the detection period after proton beam irradiation. The PET images for detection period of (a) 0, (b) 50, (c) 100, and (d) 200 s are shown.

the detection event of the activity measured in the gating window will became about one third of the total detection events, and the statistical error will increase. Therefore, the measurement was performed with no synchronization with organ motion by respiration.

Changes in the activity distribution during the treatment period

In each treatment site, the activity distribution changed probably by reduction of the tumor size and changing of the body shape was conspicuously observed in some cases of the head and neck.

The verification was performed for a case involving tumors of the head and neck. Proton beam irradiation was performed in three fields of view: Port 1: 123 MeV, 90-mm SOBP, 350° gantry angle, 0° bed angle; Port 2: 121 MeV, 90-mm SOBP, 10° gantry angle, 20° bed angle; and Port 3: 117 MeV, 80-mm SOBP, 340° gantry angle, 350° bed angle. The irradiation dose was 2.5 GyE. Figure 5 shows a calculated proton dose distribution, an activity distribution, and a depth profile of a 2.5-GyE dose irradiation after a delivery dose of 2.5 (reference image), 10.0, 17.5, or 32.5 GyE from Port 1, a delivery dose of 5.0 (reference image), 12.5, 20.0, or 35.0 GyE from Port 2, and a delivery dose of 7.5 (reference image), 15.0, 22.5, or 30.0 GyE from Port 3. Changes of the activity distribution were observed according to changes of the proton beam range and the dose delivered by previous irradiations resulted in a reduction of the tumor (see the arrow and the area surrounded by the dotted line in Fig. 5). The changing values of the activity range for each irradiation field (Port 1, Port 2, and Port 3) are shown in upper left of Fig. 6.

The activity range was defined by the depth point of 50% distal falloff in the activity distribution normalized at the iso-center. The changing value of the activity range fully exceeded a 10-mm length. Moreover, to observe the changes in the activity distribution in the depth direction in a similar manner, the ratio of the integration of the detected numbers between 20 mm and 70 mm from the iso-center was expressed as follows:

$$R(D) = \frac{\int_{20}^{70} \left(dA(D)/dZ \right) dz}{\int_{20}^{70} \left(dA(0)/dZ \right) dz}. \qquad (1)$$

Here, z is the depth, D is the delivery dose, A(D) is the depth activity distribution, and A(0) is the reference depth activity distribution. The ratio of the delivery dose is shown in the middle left of Fig. 6. The bottom left of Fig. 6 is the proton beam irradiation time per fraction dose at each irradiation. The average of the irradiation time was 30 s, and the difference of the irradiation time at random was within 3 s.

In this case, a new CT image was scanned and a retreatment planning was produced after the delivery of 35 GyE of the prescribed dose of 65 GyE. The volume of the tumor was decreased from 184 mL to 125 mL (the arrow in right of Fig. 6 shows the visible tumor reduction), and the maximum beam range was shortened by 20-mm water equivalent length. In the other 2 cases of 18 clinical cases of the head and neck, the changing activity range of more than 10 mm was observed. Similarly, the new CT image acquisition and the retreatment planning were immediately performed after the observation of the changing activity range. The reduction
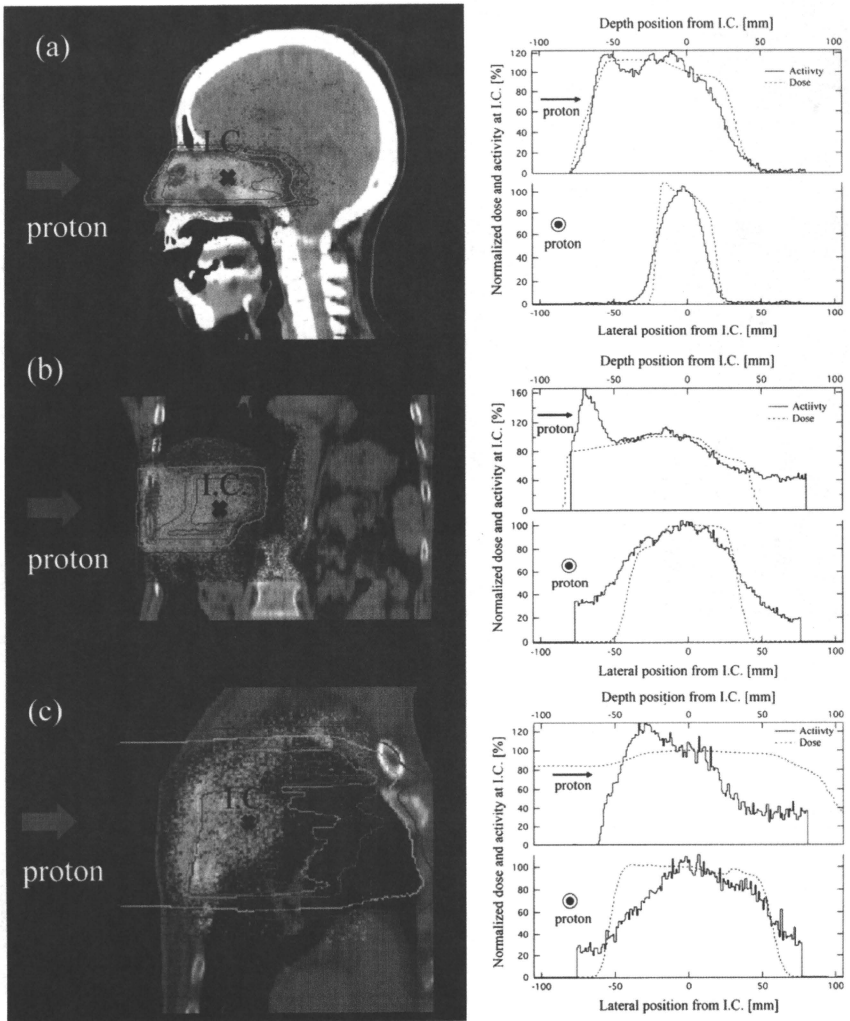
Fig. 4. The calculated dose distribution and the measured activity distribution (left figure), and corresponding lateral and depth profiles (right figure) of the irradiation fields (see Table 1) in each case involving tumors of the head and neck (a), the liver (b), the lungs (c), the prostate (d), and the brain (e), respectively. The iso-dose line of 100% is red, 80% yellowish green, 50% light blue, and 20% purple. The iso-activity wash between 30% and 100% changed from light blue to red.
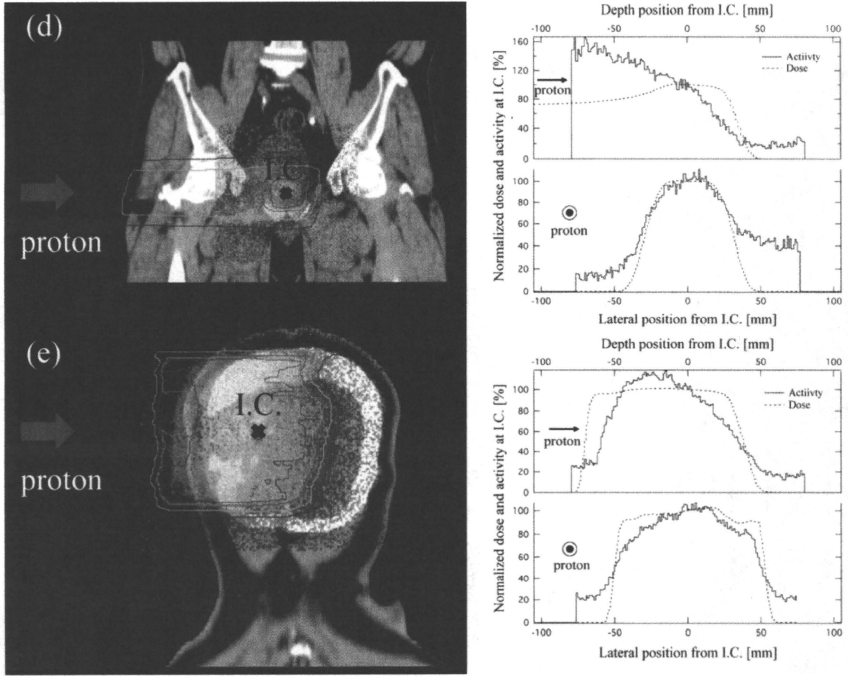
Fig. 4. (*continued*).

of the tumor's volume was more than 100 mL. Also, in carbon therapy, similar observation of the tumor shrinkage has been reported in (7). The BOLPs-RGp indicated that the proton irradiation dose was delivered to the brain stem of organs at risk.

Washout effect of the activity in the treatment period

A histopathologic examination demonstrated that higher activity was observed in regions containing necrotic liver cells than in any other region. The upper panel of Fig. 7 shows the calculated dose distribution and the measured activity distribution on a CT image taken at the first treatment of a 3.8 GyE delivery dose. The bottom left panel of Fig. 7

shows the number of detection counts per 20 s of activity in the regions of interest of areas A and B in the liver. Hence, the region of interest of area A is the necrotic region of the tumor, and area B is the normal tumor region. Therefore, area B-A is equivalent to the area of the tumor minus the necrotic region. The observed decay curves in the region of interest of area A and B-A were fitted well enough using a double exponential equation. The two half-lives of the double exponential fitting were 31 ± 8 s and 146 ± 20 s in the area A, and 21 ± 4 s and 164 ± 11 s in the area B-A, respectively. The half-life was longest in the necrotic region of the tumor. The activity images for the 200 s measurement by the BOLPs-RGp are shown in the left of Fig. 8. The high activity

Table 1. Summary of proton beam irradiation parameters

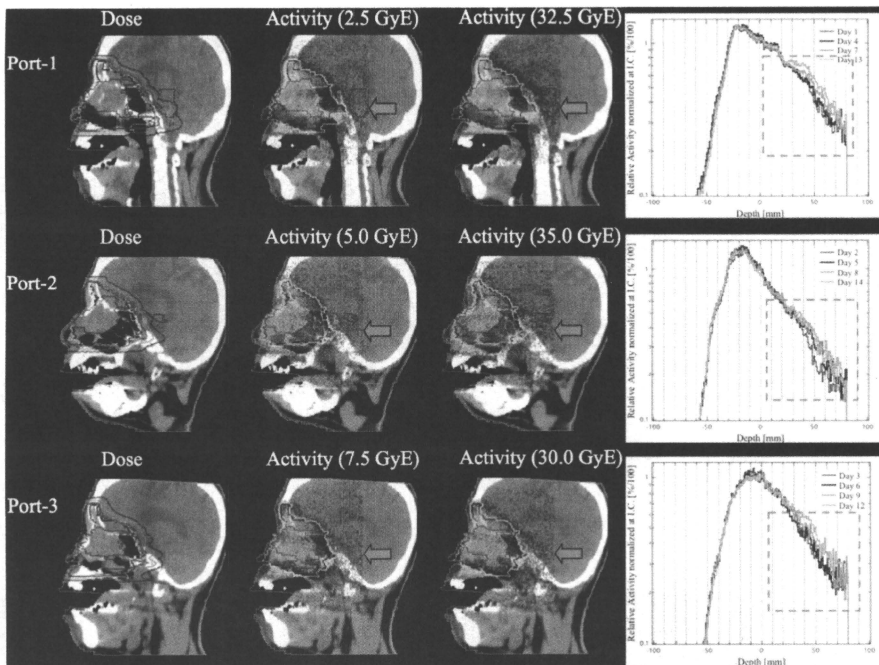|	Treatment site	Proton energy [MeV]	SOBP [mm]	Gantry angle [deg.]	Bed angle [deg.]	Fractional dose [GyE]	Irradiation time [sec.]
(a)	Head and Neck	123	90	0	0	2.5	39
(b)	Liver	137	70	270	0	3.8	229
(c)	Lungs	145	70	160	0	2.0	38
(d)	Prostate	187	50	270	0	2.0	15
(e)	Brain	122	90	330	90	2.5	40

Fig. 5. The calculated proton dose distribution, measured activity distribution of a 2.5-GyE dose irradiation, and the depth profile of the measured activity normalized to the iso-center (0-mm depth) of the reference activity after a delivery dose of 2.5–35.0 GyE.

of the necrotic region decreased to same level as the normal parts of the liver in the last treatment. The ratio F of the detection activity normalized to the activity data from the first treatment for the delivery doses in the area A and the area B-A is expressed as follows:

$$F(D) = \frac{\int_0^{S_A} (d\mathrm{N}(\mathrm{D})/d\mathrm{S})\,d\mathrm{S}/\int_0^{S_A} d\mathrm{S}}{\int_{S_A}^{S_B} (d\mathrm{N}(\mathrm{D})/d\mathrm{S})\,d\mathrm{S}/\int_{S_A}^{S_B} d\mathrm{S}}. \qquad (2)$$

Here, N is the detection number, S_A is the square of area A, and S_B is the square of area B. Ratio of the F values normalized at the value in first treatment calculated by using Eq. 2 and proton beam irradiation time per fraction dose are shown in the right of Fig. 8. The average of the irradiation time at random was 159 ± 77 s. There was no correction in the irradiation time and the decrease of the activity shown in Fig. 8. A decrease in the activity of the necrotic region was observed after the delivery dose was increased without depending on the beam irradiation time per fraction dose.

DISCUSSION

This study focused on the development of the BOLPs-RGp and its clinical use against tumors of the head and neck, liver, lungs, prostate, and brain in the proton therapy. Quick measurement of the activity generated in a patient's body after proton irradiation is feasible by using the BOLPs-RGp. The elements tracked by the activity imaging are ^{11}C (20.39 min), ^{10}C (19.26 s), ^{13}N (9.965 min), ^{15}O (122.2 s), ^{14}O (70.61 s), ^{30}P (2.498 min), and ^{38}K (7.636 min), and according to the results of a simulation by Parodi *et al.*, the "key" positron emitter nuclei are ^{11}C and ^{15}O (14). The measurement of this activity must be immediately performed after proton irradiation as the half-life of ^{15}O is about 2 min. As a result, the information for activity imaging is obtained in a short period. On the other hand, in the case of a beam OFF-LINE PET system used with a commercial based PET or PET/CT apparatus, it is very difficult to measure the activity of ^{15}O for several minutes even at the start of the activity measurement after proton irradiation. The main elements used for activity imaging are ^{15}O for measurements with
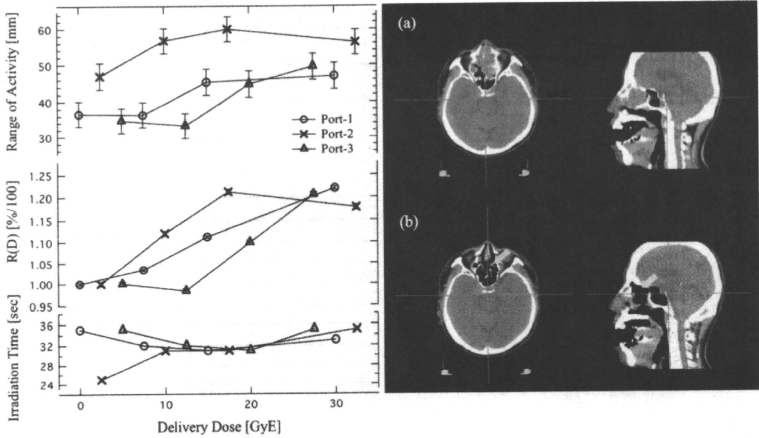
Fig. 6. Changes in the values of the activity range and proton beam irradiation time per fraction dose at each irradiation field of Port-1, Port-2, and Port-3. Axial and sagittal CT images of the head and neck before treatment (a) and after delivery doses of 35 GyE (b).
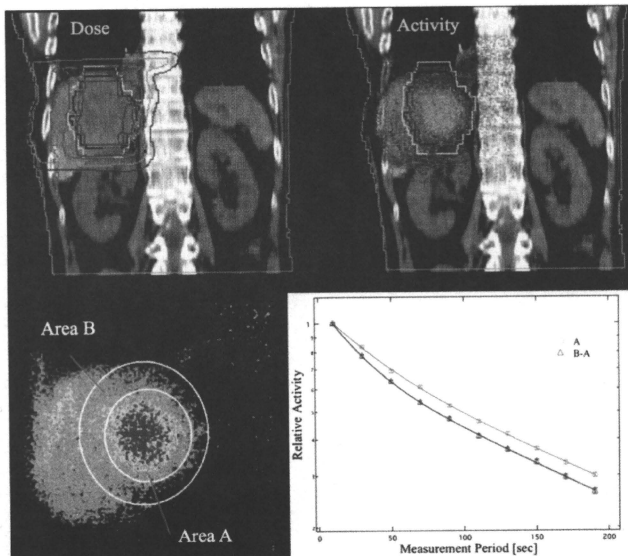

Fig. 7. The calculated dose distribution and the measured activity distribution on a CT image after the first treatment with a 3.8-GyE delivery dose, and the number of detection counts per 20 seconds of the activity in the region of interest (ROI) of areas A and B in the liver.
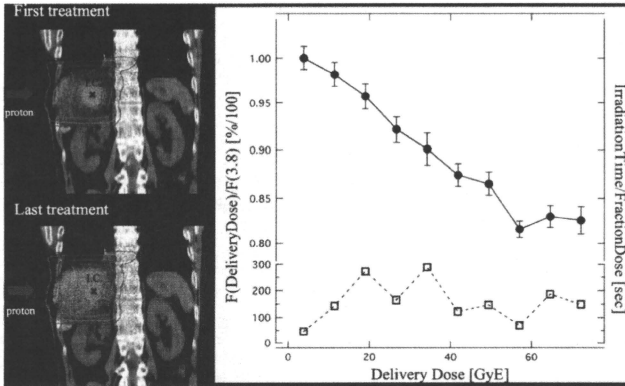
Fig. 8. The activity image and the ratio of the detection number to the measured activity calculated according to Equation (2) in the necrotic region of the liver tumor, and proton beam irradiation time per fractional dose.

the BOLPs-RGp and ^{11}C for measurements with the beam OFF-LINE PET system. As a tumor is equivalent to soft tissue, the measurement of the many [15]O nuclei generated in a tumor by proton irradiation is very important for the observation and evaluation of the changing form and the delivery dose response of the tumor. [12]C is present and ^{11}C is generated in the adipose tissue. Therefore, high activity is indicated in the region under the skin when using the beam OFF-LINE PET system. Furthermore, the BOLPs-RGp has the advantage of taking measurements with the patient in same position during proton irradiation. However, the CT image for the patient positioning can not be acquired at the same time as the activity measurement when using the BOLPs-RGp. This problem can be solved by the technological introduction of a CBCT.

At present, the length of activity measurement with the BOLPs-RGp after proton beam irradiation is 200 s; but, it may be possible that the measurement time can be shortened to less than 200 s as a result of this research. However, the measurement time must be determined with consideration to the detection efficiency by the delivery dose of each treatment site, the distance between the detector heads, and the activity measurement synchronized with the organ motion caused by respiration in the case of the liver and lungs.

The BOLPs-RGp has been used in the daily proton treatment of 48 patients. The monitoring of the accuracy of the proton beam irradiation was performed by comparing and verifying the daily activity images with reference activity images obtained at the start of the proton treatment. Specially, optimized proton treatment was performed by quickly re-planning treatment in three clinical cases involving head-and-neck tumors, because different activity distribution were observed in the two images during the treatment period. The decrease of the activity in the region of necrotic cells in the liver tumor found during the histopathological examina-tion was linked to an increase in the delivery dose. It is suggested that the increase in the washout effect in the necrotic region is caused by a decrease in the number of necrotic cells in the liver because of increased blood flow caused by the higher proton delivery dose. This effect may indicate a need to adapt the treatment to the dose response of the tumors in individual patients as well as the observation of the functional metabolism of organs.

The quality of the activity image is reduced by the large organ motion of the liver and the lungs. In cases of the prostate, the verification of changes in the activity distribution against the condition of the bladder and the position of the head of the femur will be reported in future. Moreover, a study concerning the experimental determination of cross sections of the target nuclear fragment reaction has been completed, and a simulation system that includes our cross-section data for calculating activity distribution in a patient's body with a high accuracy has been constructed using a cluster computer system. Many results of the research of the simulation have been already reported by the study group of Parodi *et al.* (12, 14). Finally, the ideal DGPT will be achieved through these developments and the research.

CONCLUSIONS

A BOLPs-RGp was constructed in our proton treatment room. The BOLPs-RGp has been used in many clinical cases. Report of the clinical use with beam ON-LINE PET or in-beam PET in the proton therapy has been never done before. The daily activity images obtained indicated the proton irradiation volume of the treatment administered to patients. Information about the positron-emitting nuclei provided by the BOLPs-RGp will be important for improving proton treatment accuracy in the future. DGPT (10) will thereby be achieved via daily proton treatment using the BOLPs-RGp.

REFERENCES

1. Oelfke U, Lam G, Atkins M. Proton dose monitoring with PET: Quantitative studies in Lucite. *Phys Med Biol* 1996;41: 177–196.

2. Litzenberg DW, Roberts DA, Lee MY, *et al.* On-line monitoring of radiotherapy beams: Experimental results with proton beams. *Med Phys* 1999;26:992–1006.

3. Parodi K, Enghardt W. Potential application of PET in quality assurance of proton therapy. *Phys Med Biol* 2000;45:N151–N156.

4. Nishio T, Ogino T, Shimbo M, *et al.* Distributions of b+ decayed nucleus produced from the target fragment reaction in $(CH_2)n$ and patient liver targets by using a proton beam for therapy. *Abstr XXXIV PTCOG Mtg Boston* 2001;15–16.

5. Parodi K, Enghardt W, Haberer T. In-beam PET measurements of β^+ radioactivity induced by proton beams. *Phys Med Biol* 2002;47:21–36.

6. Hishikawa Y, Kagawa K, Murakami M, *et al.* Usefulness of positron-emission tomographic images after proton therapy. *Int J Radiat Oncol Biol Phys* 2002;53:1388–1391.

7. Enghardt W, Parodi K, Crespo P, *et al.* Dose quantification from in-beam positron emission tomography. *Radiother Oncol Suppl* 2 2004;73:S96–S98.

8. Nishio T, Sato T, Kitamura H, *et al.* Distributions of β^+ decayed nuclei generated in the CH_2 and H_2O targets by the target nuclear fragment reaction using therapeutic MONO and SOBP proton beam. *Med Phys* 2005;32:1070–1082.

9. Parodi K, Ponisch F, Enghardt W. Experimental study on the feasibility of in-beam PET for accurate monitoring of proton therapy. *IEEE Trans Nucl Sci* 2005;52:778–786.

10. Nishio T, Ogino T, Nomura K, *et al.* Dose-volume delivery guided proton therapy using beam ON-LINE PET system. *Med Phys* 2006;33:4190–4197.

11. Parodi K, Paganetti H, Cascio E, *et al.* PET/CT imaging for treatment verification after proton therapy: A study with plastic phantoms and metallic implants. *Med Phys* 2007;34: 419–435.

12. Parodi K, Paganetti H, Shih HA, *et al.* Patient study of in vivo verification of beam delivery and range, using positron emission tomography and computed tomography imaging after proton therapy. *Int J Radiat Oncol Biol Phys* 2007;68:920–934.

13. Nishio T, Miyatake A, Inoue K, *et al.* Experimental verification of proton beam monitoring in a human body by use of activity image of positron-emitting nuclei generated by nuclear fragmentation reaction. *Radiol Phys Technol* 2008;1: 44–54.

14. Parodi K, Ferrari A, Sommerer F, *et al.* Clinical CT-based calculations of dose and positron emitter distributions in proton therapy using the FLUKA Monte Carlo code. *Phys Med Biol* 2007;52:3369–3387.

15. Pawelke J, Enghardt W, Haberer T, *et al.* In-beam PET imaging for the control of heavy-ion tumour therapy. *IEEE Trans Nucl Sci* 1997;44:1492–1498.

16. Parodi K, Crespo P, Eickhoff H, *et al.* Random coincidences during in-beam PET measurements at microbunched therapeutic ion beams. *Nucl Instrum Meth A* 2005;545:446–458.

17. Uchida H, Okamoto T, Ohmura T, *et al.* A compact planar positron imaging system. *Nucl Instr Meth* 2004;A516:564–574.

ELSEVIER

High−dose rate brachytherapy alone in postoperative soft tissue sarcomas with close or positive margins

Jun Itami[1,*], Minako Sumi[1], Yasuo Beppu[2], Hirokazu Chuman[2], Akira Kawai[2], Naoya Murakami[1], Madoka Morota[1], Hiroshi Mayahara[1], Ryoichi Yoshimura[1], Yoshinori Ito[1], Yoshikazu Kagami[1]

[1]Department of Radiation Oncology, National Cancer Center Hospital, Tokyo, Japan
[2]Department of Orthopaedics, National Cancer Center Hospital, Tokyo, Japan

ABSTRACT PURPOSE: In the management of soft tissue sarcomas, perioperative radiation therapy has been
used to reduce the risk of local recurrence after resection. However, a significance of postoperative
high−dose rate brachytherapy (HDRBT) remains to be studied. Retrospective analysis was per-
formed to elucidate the role of postoperative HDRBT.
METHODS AND MATERIALS: Twenty-five patients with 26 soft tissue sarcoma lesions under-
went postoperative HDRBT using ^{192}Ir remote afterloader without external beam radiation therapy.
Ninety-two percent of the lesions were Grade 2 or 3 malignancies, and 50% were resected with
positive surgical margins. The remaining 50% had very close margins. Fourteen lesions were
treated for local recurrences after previous resections. Applicators of HDRBT were placed during
the operation to include only the tumor bed excluding surgical scars. Applied dose was mainly
36 Gy/6 fractions/3 d b.i.d.
RESULTS: Five-year local recurrence-free survival was 78.2% in all the 26 lesions. Recurrences
were not seen within the treated volume of HDRBT. Two groups were defined according to the
marginal status and number of previous operations. Group 1 was the lesions with a positive margin
and foregoing resections. The remaining lesions were classified as Group 2. Five-year local
recurrence-free survival was 43.8% and 93.3% in Group 1 and Group 2, respectively with a statis-
tically significant difference ($p = 0.004$).
CONCLUSIONS: Postoperative HDRBT was effective in controlling local lesions; but in Group 1
lesions, addition of a wide field external beam radiation therapy seems to be necessary to improve
the local control rate. © 2010 American Brachytherapy Society. Published by Elsevier Inc. All
rights reserved.

Keywords: High−dose rate brachytherapy; Soft tissue sarcoma; Postoperative radiation

Introduction

In the management of soft tissue sarcomas (STSs), surgical resection is the mainstay of treatment. However, local recurrence is seen frequently, especially in the patients with positive surgical margins, a large tumor, and/or recurrence after foregoing surgery (1, 2). Post- or preoperative radiation therapy has been demonstrated to

be effective in reducing the risk of local recurrence (2−4). Furthermore, the combination of surgery and perio-perative radiation therapy has changed the management policy of the STSs from a mutilating radical amputation to limb-sparing therapy. External beam radiation therapy (EBRT) is the most frequently used method of radiation therapy, whereas postoperative radiation therapy using low−dose rate brachytherapy (LDRBT) has been reported to be also effective in lowering the local recurrence rate (3, 5). In contrast, postoperative high−dose rate brachytherapy (HDRBT) of STS has been published only sporadically and its clinical significance in the management of STSs remains to be studied (6−10). In National Cancer Center Hospital, HDRBT has been used without EBRT in the post-operative radiation therapy of patients with STSs, whose

removal seemed to result in a resection with positive or close margins. In this study, the role and significance of postoperative HDRBT alone in the management of STS is analyzed retrospectively.

Methods and materials

From 1995 to 2008, 25 patients with 26 STS lesions underwent postoperative HDRBT alone in National Cancer Center Hospital. There were 10 men and 15 women. In a male patient with malignant fibrous histiocytoma, the lesion was managed with operation and postoperative HDRBT and the tumor recurred proximal to the original site. The recurred tumor was resected and postoperative HDRBT was administered repeatedly (Table 1). Median age was 60.7 years ranging from 9 to 76 years. Primary sites of the tumors were upper extremity with 12 lesions and lower extremity with 11 lesions. Primary truncal STS was seen in three lesions. As for pathology, malignant

Table 1
Age and sex of the 25 patients and characteristics of the 26 lesions undergoing postoperative high—dose rate brachytherapy for soft tissue sarcomas

Characteristics	Number
Median age (y)	60.7 (range, 9—76)
Sex	
Male:female	11:15
Primary Site	
Upper extremity	12
Lower extremity	11
Trunk	3
Histopathology	
Malignant fibrous histiocytoma	12
Leiomyosarcoma	3
Synovial sarcoma	3
Liposarcoma	2
Rhabdomyosarcoma	2
Others	4
Malignant grade	
1	2
2	9
3	15
Tumor size	
Mean	9 cm (range, 1.2—22)
<5 cm	9
>5 cm	17
Number of previous operations	
0	12
>1	14
Status of surgical margin	
Positive	13
Negative	13
Chemotherapy	
Yes	12
No	14

fibrous histiocytoma was most frequently seen in 12 lesions followed by leiomyosarcoma in three lesions. Eighty-eight percent of lesions were diagnosed as Grade 2 or 3 in three-tiered grade classification. Surgical margins were microscopically positive for sarcoma cells in 13 lesions; whereas in 13 lesions, resection margins were very close (less than 5 mm) to the tumor because vicinity of the tumor to the functionally important structures, such as major neurovascular bundles, made it difficult to attain adequate surgical margins. The maximal tumor size in the pathologic specimen was 9 cm with a range between 1.2 cm and 22 cm. Included in the present study were also the STSs, which recurred after previous surgeries. Fourteen lesions were treated by resections and HDRBTs for recurrences after the previous surgeries. Number of the foregoing surgeries ranged from one to eight.

Indication of the postoperative HDRBT was determined preoperatively by a joint meeting of orthopedic surgeons and radiation oncologists. Postoperative HDRBT was used to preserve major neurovascular bundles or major muscles, which are indispensable to maintain the functional integrity of extremities. During the operation, resection margins close to or contaminated by tumor were confirmed by both orthopedic surgeons and radiation oncologists. Surgical clips were placed to delineate the tumor bed as well as the resection margins very close to the lesion. The flexible applicator tubes of HDRBT were placed to cover the tumor bed with 1—2 cm margins in a parallel fashion with 1—1.5 cm intervals between the tubes. Applicator tubes have a closed end and were sutured to the tumor bed. The open ends of tubes were pulled through the skin and connected to the remote afterloading machine. Muscular or adipose tissue flaps of about 5 mm thickness were used to cover major nerve and/or vascular bundles to avoid direct contact of the applicators. The tubes were removed after completion of the HDRBT. Radiation therapy planning was performed by Plato (version 14.3.7; Nucletron, Veenendaal, The Netherlands). The coordinates of the tube applicators were digitized using orthogonal x-rays and/or CT images. The dwell positions of HDRBT source were located to cover tumor bed encircled by the surgical clips. No special efforts were exerted to include all the scar and drainage sites. Geometric optimization was used to calculate dwell times with a reference poinof 5 mm lateral to the midportion of the central tube applicator. For HDRBT, ^{192}Ir afterloading machine was used (microSelectron HDR; Nucletron, Veenendaal, The Netherlands). All the lesions but one were irradiated with a fractional dose of 6 Gy, and the remaining one was treated by 4.5 Gy because neighboring nerve could not be adequately protected by the flap. The HDRBT was done b.i.d. with an interval between the fractions of at least 6 h. Six fractions were administered in all but one lesion, which was treated with four fractions because of the accidental early slip out of the applicators. In 24 lesions, applied dose was 36 Gy, 30 Gy, and 27 Gy each in one lesion (Table 2). Interval

Table 2
Postoperative high—dose rate brachytherapy for soft tissue sarcomas

Characteristics	Number
Interval between OP and BT (days)	
Mean	5.3 (range, 1—7)
<5	2
>5	24
Median number of applicators	7 (range, 2—15)
Fractional dose	
4.5 Gy	1
6 Gy	25
Number of fractions	
5	1
6	25
Total dose (EQD2 for tumor control)	
27 Gy (32.6 Gy)	1
30 Gy (40 Gy)	1
36 Gy (48 Gy)	24
Mean volume encircled by the prescribed dose	74.9 cc (range, 18.5—173)

OP = operation; BT = brachytherapy; EQD2 = equivalent dose with 2 Gy fraction.

between the operation and the HDRBT was 5.3 days in a mean, and 24 HDRBTs were commenced between 5 and 7 days after the operation. Number of implanted tube applicators ranged from two to 15 with a median of seven. The treated volume encircled by the prescribed dose ranged from 18.5 to 173 cc with a mean of 74.9 cc. Chemotherapy was delivered in 12 lesions.

Median followup length was 49.7 months ranging from 4.7 to 187 months. Local recurrence-free survival (LRFS) was calculated in the 26 lesions, and overall survival (OS) in all the 25 patients. Local recurrence was defined as a regrowth of the STS within 5 cm from the operation scars. LRFS and OS were calculated by Kaplan—Meier method (11) with a difference between the survival curves evaluated by a logrank test. Acute morbidities seen within 6 months after HDRBT were classified according to the National Cancer Institute Common Terminology Criteria for Adverse Events version 3.0, whereas Radiation Therapy Oncology Group/European Organization for Research and Treatment for Cancer criteria were used for late morbidities (12).

Results

Local recurrence was observed in five lesions. All the local recurrences occurred outside of the treated volume of HDRBT. These local recurrences were within the treated volume, if postoperative EBRT were administered encompassing all the surgical scars with 5 cm margins. LRFS of all 26 lesions was 78.2% in 5 years. According to the surgical margin status, 5-year LRFSs of positive and negative margins were 90.9% and 64.6%, respectively, without
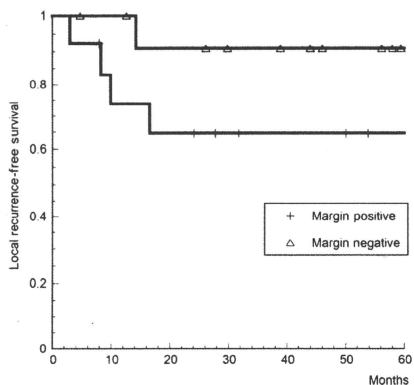

Fig. 1. Local recurrence-free survivals according to surgical margin status.

a statistically significant difference ($p = 0.11$) (Fig. 1). In the lesions treated as a primary therapy, LRFS is 90.9% in 5 years, whereas the recurrent lesions after previous operations showed 5-year LRFS rate of 66.5% ($p = 0.15$) (Fig. 2). The lesions were classified into two groups according to the surgical margin status and number of foregoing operations. Group 1 was defined as recurrent lesions, which were resected with positive surgical margins. All other lesions were classified into Group 2. There were eight lesions in Group 1 and 18 in Group 2. Five-year LRFS was 43.8% and 93.3% in Group 1 and Group 2, respectively
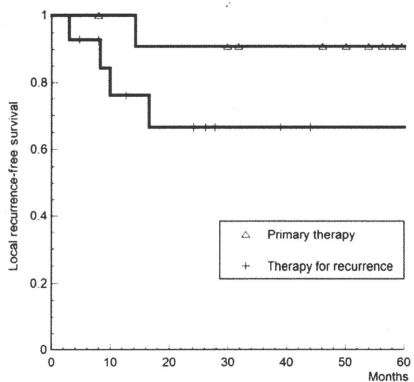

Fig. 2. Local recurrence-free survivals according to number of previous operations.